Performance evaluation of different implementations of the Lagrangian speckle model estimator for non-invasive vascular ultrasound elastography

Elizabeth Mercure
Laboratory of Biorheology and Medical Ultrasonics, Research Center, University of Montreal Hospital, Montreal, Quebec H2L 2W5, Canada

Guy Cloutier
Laboratory of Biorheology and Medical Ultrasonics, Research Center, University of Montreal Hospital, Montreal, Quebec H2L 2W5, Canada, Institute of Biomedical Engineering, University of Montreal, Montreal, Quebec H3T 1J4, Canada, and Department of Radiology, Radio-Oncology and Nuclear Medicine, University of Montreal, Montreal, Quebec H2L 4M1, Canada

Cédric Schmitt
Laboratory of Biorheology and Medical Ultrasonics, Research Center, University of Montreal Hospital, Montreal, Quebec H2L 2W5, Canada and Institute of Biomedical Engineering, University of Montreal, Montreal, Quebec H3T 1J4, Canada

Roch L. Maurice[a)]
Laboratory of Biorheology and Medical Ultrasonics, Research Center, University of Montreal Hospital, Montreal, Quebec H2L 2W5, Canada, Institute of Biomedical Engineering, University of Montreal, Montreal, Quebec H3T 1J4, Canada, and Department of Radiology, Radio-Oncology and Nuclear Medicine, University of Montreal, Montreal, Quebec H2L 4M1, Canada

(Received 20 November 2007; revised 24 April 2008; accepted for publication 24 April 2008; published 16 June 2008)

Non-invasive vascular ultrasound elastography (NIVE) was recently introduced to characterize mechanical properties of carotid arteries for stroke prevention. Using the Lagrangian speckle model estimator (LSME), the four components of the 2D deformation matrix (Δ), which are the axial strain (Δ_{yy}) and shear (Δ_{yx}) and the lateral strain (Δ_{xx}) and shear (Δ_{xy}), can be computed. This paper overviews four different implementations of the LSME and addresses their reliability. These implementations include two unconstrained (L&M and L&M$^+$) and one constrained (ITER^c) iterative algorithms, and one optical flow-based (OF-based) algorithm. The theoretical frameworks were supported by biomechanical simulations of a pathology-free vessel wall and by one single layer vessel-mimicking phantom study. Regarding simulations, the four LSME implementations provided similar biases on axial motion parameters, except the L&M that outperformed other methods with a minimum strain bias of -3%. LSME axial motion estimates showed good consistence with theory, namely the OF-based algorithm that in a specific instance estimated Δ_{yy} with no relative error on the standard deviation. With regards to lateral motion parameters, ITER^c exhibited a minimum strain bias of -8.5% when ultrasound beam and motion mostly run parallel, whereas L&M performs strain and shear estimates with less than 23% bias independently of orientations. The *in vitro* vessel phantom data showed LSME Δ_{yy} and Δ_{yx} maps that were qualitatively equivalent to theory, and noisy Δ_{xx} and Δ_{xy} elastograms. In summary, the authors propose to promote the OF-based LSME as an optimal choice for further applications of NIVE, because of its reliability to compute both axial strain and shear motion parameters and because it outperformed the other implementations by a factor of 30 or more in terms of processing time. © *2008 American Association of Physicists in Medicine*. [DOI: 10.1118/1.2936771]

Key words: atherosclerosis, biomechanical simulations, Lagrangian speckle model estimator (LSME), non-invasive vascular ultrasound elastography (NIVE), shear, strain, vessel-mimicking phantom

NOMENCLATURE

- AT = affine transformation of coordinates
- Δ = 2D deformation matrix
- E = Young's modulus
- $H(x,y)$ = 2D point-spread function of the ultrasound imaging system
- I = 2D identity matrix
- $I(x(t),y(t))$ = radio-frequency (RF) image at time t
- $I_{\mathrm{Lag}}(x(t),y(t))$ = Lagrangian speckle image at time t
- J_k = Jacobian matrix
- LT = linear transformation matrix
- m_i, $i \in \{1,\ldots,6\}$ = components of [LT] $\cup$ components of [Tr]

m_7 = contrast parameter of $I(x(t),y(t))$
m_8 = brightness parameter of $I(x(t),y(t))$
$n(x(t),y(t))$ = additive noise term
P_b = blood pressure
R_i and R_o = inner and outer radii of the blood vessel, respectively
$\Re(x(t),y(t))$ = error term
TR = translation vector
$Z(x,y)$ = 2D acoustic impedance function

I. INTRODUCTION

Atherosclerosis is the leading cause of death in industrialized countries.[1] This disease is characterized by the accumulation of lipids, calcium, cellular debris, and white blood cells within the inner lining of an artery and results in plaque formation. Its development generates a thickening and a hardening of the artery. Plaques can become large enough to form stenoses or they can become fragile and rupture. Typically, a large lipid core covered by a thin fibrous cap defines an unstable or vulnerable plaque with a high risk of rupture.[2] In carotid arteries, plaque rupture leads to the formation of blood clots that can partially or totally obstruct the vessel lumen at the site of rupture or distally from this site and lead to strokes. Hence, the identification of such vulnerable plaques is of crucial clinical importance.

Several studies have shown that the phenomenon of plaque enlargement was associated with an increase of the fluid shear stress, i.e., the stress induced by the blood flow at the inner layer of the artery wall.[3–6] The authors then assumed that high wall shear stress could produce a thinning of the fibrous cap and thus create a rupture-prone vulnerable plaque. A close correlation between the maximum shear stress and the site of rupture was observed in human carotid plaques.[6] Furthermore, the occurrence of shear stress within the normal arterial wall of many arteries, such as the carotid, was recently demonstrated and the hypothesis that the long-term effect of this flow shear stress could weaken a material and increase its risk of rupture was proposed.[7]

Based on intravascular ultrasound (IVUS), endovascular elastography (EVE) was introduced to assess arterial wall mechanical properties.[8–14] Using conventional IVUS catheters, time-sequences of 2D radio-frequency (RF) data are recorded. Strain images, or elastograms, are then computed, the intraluminal compression/dilatation being induced either by the cardiac pulsation or the pressure inferred by a compliant intravascular angioplasty balloon. de Korte *et al.*,[12] Schaar *et al.*,[15] and more recently Maurice *et al.*[14,16] demonstrated that EVE was able to dissociate different plaque components. Interestingly, coronary artery plaques that were assumed to embed lipid cores were identified. However, to circumvent the invasiveness of catheter-based methods, non-invasive vascular elastography (NIVE) was recently proposed to characterize superficial arteries.[17–23] Usually, time-sequences of RF data are transcutaneously recorded to assess the vascular tissue motion induced by the blood flow pulsation. Meanwhile, the acoustic radiation force impulse (ARFI) imaging was also proposed for NIVE applications.[24,25] Such a method uses short-duration impulses of relatively high energy to generate tissue kinematics. Displacement fields are then assessed using correlation-based methods, whereas local tissue stiffness is deduced from relative amplitudes of axial displacements.

The NIVE method, reported in this paper, was implemented using the Lagrangian speckle model estimator (LSME). Unlike most estimators that can be found in the literature, the LSME was formulated as a nonlinear minimization problem that allows assessing the complete 2D-deformation matrix (axial strain, axial shear, lateral strain, and lateral shear). While strain components dictate the rigidity of the vascular materials (soft and hard), shear components may give insights about plaque vulnerability by indicating plaque prone-to-rupture in regions subjected to high stresses. Interestingly, high shear stresses and equivalently high shear strains can be expected to mainly occur at interfaces between soft and hard regions as it could be the case between lipid cores and fibrotic caps. Whereas preliminary NIVE results were recently reported,[23] the main objective of this study was to investigate the reliability of the 2D-deformation matrix (Δ) using biomechanical simulations and vessel-mimicking phantom data. Four different implementations of the LSME, which include two unconstrained (L&M and L&M$^+$) and one constrained (ITER^c) iterative algorithms, and one optical flow-based (OF-based) algorithm, were evaluated. Comparisons between LSME implementations were performed in terms of bias and relative error on the standard deviation for every Δ component and also in terms of relative computation time differences. It is worth mentioning that the choice of the LSME for NIVE applications was motivated by the fact that this estimator allows simultaneous assessment of strain and shear deformations.

II. MATERIALS AND METHODS

II.A. Biomechanical simulations

To evaluate the reliability of the LSME motion estimates, a homogeneous, i.e., a plaque-free arterial wall, was investigated. The geometry and kinematics were simulated according to the exact solution of a pressurized thick-wall cylindrical blood vessel embedded in an elastic coaxial cylindrical medium. Assuming an infinite medium, the components of the deformation matrix Δ are given by[21]

$$\Delta(x,y)=\begin{bmatrix} K\dfrac{y^2-x^2}{(x^2+y^2)^2} & -2K\dfrac{xy}{(x^2+y^2)^2} \\ -2K\dfrac{xy}{(x^2+y^2)^2} & K\dfrac{x^2-y^2}{(x^2+y^2)^2} \end{bmatrix} \quad \text{with} \quad K = \frac{3}{2}P_b\left[E^{(1)}\left(\frac{1}{R_i^2}-\frac{1}{R_o^2}\right)+\frac{E^{(2)}}{R_o^2}\right]^{-1}, \tag{1}$$

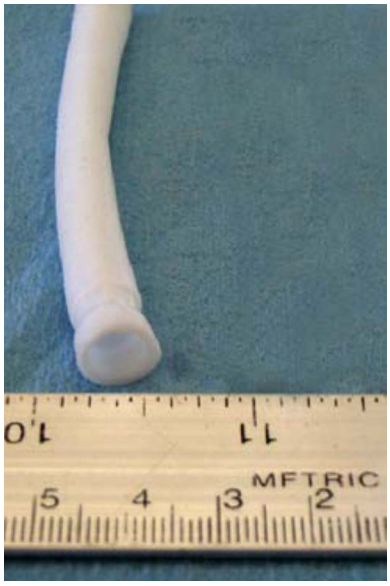

FIG. 1. Picture of the vessel-mimicking phantom.

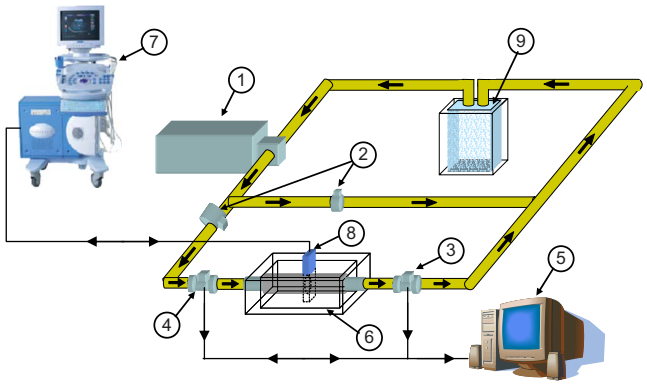

FIG. 2. Schematic illustration of the experimental setup with (1) indicating the pulsing pump, (2) the two manual hydraulic valves, (3) the pressure monitor, (4) the electromagnetic flowmeter, (5) the computer, (6) the phantom reservoir, (7) the ultrasound acquisition system, (8) the linear array ultrasound probe, and (9) the water reservoir.

where superscripts (1) and (2) represent the vessel wall and the external medium, respectively. P_b defines the blood pressure, E gives the Young's modulus, while R_i and R_o are the inner and outer radii of the blood vessel, respectively. In addition, (x,y) describes the lateral (x) and axial (y) orientations of the image plane, respectively, with the coordinate system origin being at the lumen center of the cross-sectional vessel area. It is worth remembering that the axial orientation is conventionally associated with the ultrasound beam propagation direction, whereas the lateral orientation is orthogonal to that of the beam propagation. To respect the vessel-mimicking phantom characteristics described below, and with the purpose of simulating an adult human atherosclerosis-free common carotid artery, R_i and R_o were set to 3.01 and 4.59 mm, respectively, providing a 1.58 mm wall thickness.[26,27] E was 91 kPa for the vascular tissue and 1 kPa for the external medium, as to minimize the external constraint on the vessel wall. Based on physiological parameters (heart rate of 70 beats per minute and pulse pressure gradient of 40 mm Hg) and assuming a frame rate of 19 images per second for the ultrasound system, the intraluminal pressure gradient (P_b) between two successive RF images was set to 5 mm Hg (0.67 kPa). Note that the LSME implementations of NIVE are based on the estimation of deformations from successive or interleaved RF images.

II.B. Phantom experiment description

The phantom experiment was designed prior to the biomechanical simulations as to provide similar geometry, mechanics, physiology, and acoustic parameters. As illustrated in Fig. 1, the phantom mimicked a single-layer vessel wall. Following the manufacturing description,[28] it consisted of a three freeze-thaw cycle polyvinyl alcohol cryogel (PVA-C) material for which E was estimated at 91 ± 13 kPa. The solution was made of a concentration of 10% by weight of PVA dissolved in pure water (CAS 7732-18-5) and ethenol homopolymer (CAS 9002-89-5).

The experimental setup that was used to stress the inner wall and induce vascular tissue deformation is illustrated in the block-diagram of Fig. 2. To summarize, a pulsating intraluminal pressure was applied within the lumen of the vascular phantom with a pulsing pump (model 1421 blood pump, Harvard Apparatus Inc., Holliston, MA, USA; label 1). The pressure and the flow (made of degassed water at room temperature) were regulated with two valves (2) and were measured by a pressure monitor (model E102, Medical Data Electronics, Arleta, Ca, USA; label 3) and an electromagnetic flowmeter (Cliniflow II, model FM 701D, Carolina Medical, King, NC, USA; label 4), respectively. The pressure and flowmeter monitors were connected to an acquisition system (5). The PVA-C vessel was positioned between two watertight connectors, in a Plexiglas box also filled with degassed water (6) at room temperature. Rubber o-rings were used to tighten the vessel-mimicking phantom onto Plexiglas tubes at both extremities. Cross-sectional RF images were acquired with the Sonix RP scanner (Ultrasonix, Vancouver, Canada; label 7) that was equipped with a 7 MHz linear array probe (8) and had a frame rate of 19 images per second. Similarly to biomechanical simulations, the elastograms were computed for a pressure gradient of 5 mm Hg between pair of RF images. To minimize decorrelation artifacts due to flow pulsation, RF data recorded at end-diastole were investigated.

II.C. The Lagrangian speckle model estimator (LSME)

II.C.1. Theoretical concept

The premise of any ultrasound-based tissue-motion estimator is that the "speckle" pattern, on average, reproduces the underlying tissue motion. However, the vascular tissue is heterogeneous, and its kinematics is known to be complex provided it is subjected to rigid and nonrigid rotations, scaling, shear, etc. In such cases, the relative movement of scatterers induces changes in the amplitude and phase of the

backscattered wavelets. This phenomenon is largely responsible for morphological changes of the speckle over time, and hence significantly contributes to decorrelation noise. Whereas not discussed here, out-of-plane motion also increases decorrelation noise.

Tissue kinematics is usually described in a Eulerian coordinate system, i.e., the observer's coordinate system, also called the image coordinate system. Nevertheless, based on the decorrelation concept reported above, it can be convenient to represent the speckle as a continuum of a material property. Accordingly, the Lagrangian coordinate system, also known as the material coordinate system, was introduced to describe speckle kinematics.[29] Let us define $I(x(t),y(t))$ as the speckle pattern at a given time "t." The kinematics of $I(x(t),y(t))$ can be described using its material derivative, that is,

$$\frac{dI(x(t),y(t))}{dt} = \nabla I \cdot \vec{U} + \frac{\partial I}{\partial t} = \frac{\partial I}{\partial x}\frac{dx}{dt} + \frac{\partial I}{\partial y}\frac{dy}{dt} + \frac{\partial I}{\partial t} = I_x\frac{dx}{dt} + I_y\frac{dy}{dt} + \frac{\partial I}{\partial t}. \quad (2)$$

In this equation, also known as optical flow (OF) in computer vision,[30] dI/dt is the total derivative that expresses the rate of change for $I(x(t),y(t))$ of a "material point" (x,y) as it moves to $(x+\delta x, y+\delta y)$ in $[t,t+\delta t]$ interval of time. On the other hand, the partial derivative $\partial I/\partial t$ gives the rate of change for $I(x(t),y(t))$ at a fixed observation point (x,y).

II.C.2. Tissue motion model

Within small regions of interest (ROI), also called measurement-windows, tissue motion between two consecutive images for a short time interval "δt" can be assumed affine and Eq. (2) can be rewritten as

$$dI(x(t),y(t)) = I_x[m_1 + m_2x + m_3y] + I_y[m_4 + m_5x + m_6y] + (I(x(t+\delta t),y(t+\delta t)) - I(x(t),y(t))). \quad (3)$$

In this context, the trajectory of a given material point moving from (x,y) to $(x+\delta x, y+\delta y)$ in $[t,t+\delta t]$ interval of time can be formulated as

$$\begin{bmatrix} dx \\ dy \end{bmatrix} = \underbrace{\begin{bmatrix} m_1(t) \\ m_4(t) \end{bmatrix}}_{\mathrm{TR}} + \Delta(t)\begin{bmatrix} x \\ y \end{bmatrix} \quad \text{with}$$

$$\Delta(t) = \begin{bmatrix} m_2(t)-1 & m_3(t) \\ m_5(t) & m_6(t)-1 \end{bmatrix} = \mathrm{LT} - \begin{bmatrix} 1 & 0 \\ 0 & 1 \end{bmatrix}, \quad (4)$$

where Δ is the 2D-deformation matrix, and the vector [TR] and the matrix [LT] represent the translation and the linear geometrical transformation of coordinates of the affine transformation, respectively. Therefore, Δ_{xx} is the lateral strain, Δ_{yy} is the axial strain, and Δ_{xy} and Δ_{yx} are the lateral and axial shear parameters, respectively.

II.C.3. Image-formation model

The image-formation model reported here was widely described elsewhere.[31,32] Along with the tissue-motion model, it constitutes the framework of the LSME.[21,29] Assuming that the image formation can be modeled as a linear and space-invariant operation on a scattering function, the image at time "t" in a time-sequence of RF data can be expressed by

$$I(x(t),y(t)) = H(x,y) \otimes Z_{\mathrm{LT}(t)}(x,y) + n(x(t),y(t)), \quad (5)$$

where $Z(x,y)$ is the acoustic impedance function that was modeled, for the purpose of simulations, as a white Gaussian noise.[33] Note that, in this representation, $Z(x,y)=Z_{\mathrm{LT}(t=0)}(x,y)$, i.e., no geometrical transformation of coordinates was applied at $t=0$. [LT] is the 2D linear transformation matrix defined in Eq. (4), and $\otimes$ is the 2D convolution operator. $H(x,y)$ is the point-spread function (PSF) generated as a 1D cosine modulated by a 2D-Gaussian envelope. $n(x(t),y(t))$ is an additive noise term that is assumed to be independent and uncorrelated with the signals.[29]

Time-sequences of RF images were simulated using Eq. (5). The image-formation was described in detail elsewhere[21] and can be summarized as follows. The Matlab software (The MathWorks Inc., MA, USA, ver. 6.5) was used to generate a 2D-scattering function representing the acoustical properties of a vessel, $Z(x,y)$. The lateral and axial displacement fields obtained with the analytical solution (Sec. II A) were applied upon $Z(x,y)$ to form $Z_{\mathrm{LT}(t)}(x,y)$, representing the scattering function of the tissue moving as a function of time t. Then, $Z(x,y)$ and $Z_{\mathrm{LT}(t)}(x,y)$ were convolved with the PSF, $H(x,y)$, to provide time-sequences of RF images, $I(x(t),y(t))$. The PSF parameters were chosen to correspond to the specifications of the Sonix RP scanner (7 MHz probe, RF signal sampling frequency of 40 MHz). The signal-to-noise ratio (SNR) was fixed to 20 dB, which is close to *in vivo* RF data recorded with the Ultrasonix apparatus (22.95 dB). (This SNR was measured from *in vivo* RF data recorded from a human common carotid.) All simulated images measured 35×19 mm^2, which corresponds to 1818 samples axially $\times128$ RF lines laterally.

II.C.4. The Lagrangian speckle image (LSI)

The complex kinematics (rigid and nonrigid rotations, shear, scaling, etc.) of pathological vascular tissues set a fundamental limitation to correlation-based tissue motion estimators, if they are not appropriately compensated for. In conventional elastography, where an external compression is induced, Ophir *et al.*[34] proposed to partially compensate for scaling by using temporal stretching of the post-motion signals, whereas Chaturvedi *et al.*[35,36] proposed the 2D-companding method. In these methods, the axial tissue deformation (Δ_{yy}) map, known as axial strain elastogram, is computed from the gradient of the axial displacement field [$m_4(t)$ in Eq. (4)].

In opposition to correlation-based methods, the LSME directly assesses the deformation matrix, as given by $\Delta(t)$ in Eq. (4). For the purpose of illustration, let us consider a pair

of pre- and post-tissue-motion RF images, $I(x(t),y(t))$ and $I(x(t+\delta t),y(t+\delta t))$, respectively. The first step of the LSME consists in compensating for translation movement (TR) using cross-correlation analysis. Following that, the Lagrangian speckle image (LSI) that was introduced to describe ultrasound signals compensated for "linear" tissue motion[29] can be computed. The LSI can mathematically be formulated as

$$I_{\mathrm{Lag}}(x(t),y(t)) = [I(x(t+\delta t),y(t+\delta t))]_{\mathrm{LT}^{-1}} = H_{\mathrm{LT}^{-1}(t)}(x,y) \otimes Z(x,y) + n_{\mathrm{LT}^{-1}(t)}(x,y)|\mathrm{J}|. \quad (6)$$

In this equation, $[\mathrm{LT}^{-1}]$ is the inverse of [LT], i.e., [LT] is assumed invertible. $|\mathrm{J}|$ is the Jacobian of $[\mathrm{LT}^{-1}]$, i.e., the determinant of $[\mathrm{LT}^{-1}]$. In summary, the LSI was defined as $I(x(t+\delta t),y(t+\delta t))$ that was numerically compensated for tissue motion as to optimally resemble $I(x(t),y(t))$.[29]

II.C.5. The minimization problem

According to its definition, and also as introduced elsewhere,[37] a convenient model to formulate the LSI can be given as

$$I(x(t),y(t)) = I_{\mathrm{Lag}}(x(t),y(t)) + \Re(x(t),y(t)) = [I(x(t+\delta t),y(t+\delta t))]_{\mathrm{LT}^{-1}} + \Re(x(t),y(t)), \quad (7)$$

where $\Re(x(t),y(t))$ can be seen as an error term. The LSME can then be formulated as

$$\min_{\mathrm{LT}} \|I(x(t),y(t)) - [I(x(t+\delta t),y(t+\delta t))]_{\mathrm{LT}^{-1}}\|^2 = \mathrm{MIN}_{\mathrm{LT}} \|I(x(t),y(t)) - I_{\mathrm{Lag}}(x(t),y(t))\|^2 = \min_{\mathrm{LT}} \|\Re(x(t),y(t))\|^2. \quad (8)$$

The minimum of Eq. (8) is obtained using the appropriate [LT]. Several implementations of the LSME will briefly be described in the next sections.

II.C.6. Unconstrained iterative implementations of the LSME

Several gradient-based methods exist to numerically solve minimization problems as given by Eq. (8). In the first applications of the LSME,[21,29] tissue motion was iteratively assessed by using the Levenberg-Marquardt method (L&M).[38,39] In that context, the Jacobian matrix at the kth iteration (J_k) required to implement the L&M was computed using finite differences.[21] In the current paper, the first unconstrained iterative implementation of the LSME is referred to as the L&M method.

Because RF data are inherently noisy, the L&M strategy was not optimal with regards to its convergence. Owing to that, Maurice *et al.*[37] proposed to compute $[\mathrm{J}_k]$ using the optical flow (OF) equations. It was shown[13,37] that J_k could be expressed as

$$\mathrm{J}_k = \begin{bmatrix} \frac{\partial I_{\mathrm{Lag}}}{\partial m_1} & \frac{\partial I_{\mathrm{Lag}}}{\partial m_2} & \cdots & \frac{\partial I_{\mathrm{Lag}}}{\partial m_N} \\ \vdots & \vdots & & \vdots \\ \frac{\partial I_{\mathrm{Lag}}}{\partial m_1} & \frac{\partial I_{\mathrm{Lag}}}{\partial m_2} & \cdots & \frac{\partial I_{\mathrm{Lag}}}{\partial m_N} \end{bmatrix}. \quad (9)$$

In the above equation, m_i are motion parameters, as given by Eq. (3). $[\mathrm{J}_k]$ is an "$M \times N$" matrix, where "M" is the number of pixels in the ROI and "N" is the number of elements (six) of the affine transformation of Eq. (3). It was demonstrated by Maurice *et al.*[37] that the Jacobian matrix could be implemented as

$$\frac{\partial I_{\mathrm{Lag}}(\vec{m}^k)}{\partial \vec{m}} \cong \frac{\partial I(\vec{m}^k)}{\partial \vec{m}} = -\left\{ \frac{\partial I}{\partial x}, \frac{\partial I}{\partial x}x, \frac{\partial I}{\partial x}y, \frac{\partial I}{\partial y}, \frac{\partial I}{\partial y}x, \frac{\partial I}{\partial y}y \right\}. \quad (10)$$

In this equation, $I_{\mathrm{Lag}}(x(t),y(t))$ was rewritten as $I_{\mathrm{Lag}}(\vec{m})$, and $\vec{m}$ is the vectorization of [LT]. For the purpose of clarity in the current paper, this iterative implementation of the LSME, which uses OF equations to compute the Jacobian matrix, is referred to as L&M$^+$.

II.C.7. Constrained iterative implementation of the LSME

In both iterative implementations of the LSME reported above, speckle was assumed to be a material property that is, on average, preserved with motion, i.e., $dI(x(t),y(t))/dt=0$. A recent implementation of the LSME took into consideration potential changes of the speckle pattern.[23] This new implementation, labeled as ITER^c in the current paper, can be formulated as

$$\min_{\mathrm{AT}} \|I(x(t),y(t)) - m_7[I(x(t+\delta t),y(t+\delta t)) + m_8]\|^2, \quad (11)$$

where "AT" represents the affine transformation of Eq. (3) that includes the translation vector [TR] and the 2D linear transformation matrix [LT]. m_7 and m_8 represent contrast and brightness parameters of $I(x(t),y(t))$, respectively. This method minimizes the objection function [Eq. (11)] through an iterative process that is detailed elsewhere.[23]

II.C.8. Optical flow-based implementation of the LSME

Assuming $dI(x(t),y(t))=0$ within the measurement-windows (MWs), the discrete form of Eq. (3) can be written as

$$\begin{bmatrix} I_{x_1}x_1 & I_{x_1}y_1 & I_{x_1} & I_{y_1}x_1 & I_{y_1}y_1 & I_{y_1} \\ I_{x_2}x_2 & I_{x_2}y_2 & I_{x_2} & I_{y_2}x_2 & I_{y_2}y_2 & I_{y_2} \\ \vdots & \vdots & \vdots & \vdots & \vdots & \vdots \\ I_{x_{p\times q}}x_{p\times q} & I_{x_{p\times q}}y_{p\times q} & I_{x_{p\times q}} & I_{y_{p\times q}}x_{p\times q} & I_{y_{p\times q}}y_{p\times q} & I_{y_{p\times q}} \end{bmatrix} \begin{bmatrix} m_2 \\ m_3 \\ m_1 \\ m_5 \\ m_6 \\ m_4 \end{bmatrix} = - \begin{bmatrix} \tilde{I}_{t_1} \\ \tilde{I}_{t_2} \\ \vdots \\ \tilde{I}_{t_{p\times q}} \end{bmatrix}, \tag{12}$$

where $p \times q$ pixels are the size of the MWs. Similarly to the other implementations of the LSME, axial and lateral displacements are computed using cross-correlation and are used for rigid registration (TR compensation) before deformation (Δ) assessment. Solving Eq. (12) provides [LT] that is related to [Δ] following Eq. (4). This OF-based implementation of the LSME does not require any iterative computation, so it significantly improves the processing time. It was labeled OF-based in this study.

II.C.9. LSME implementation parameters

For each LSME implementation, the measurement-window was set at 1540×2969 μm^2, that is 80 samples axially $\times$ 20 RF lines laterally with 94% and 90% axial and lateral overlaps, respectively. No post-processing was applied to the elastograms.

II.D. Reliability of the LSME motion estimates

The reliability of the LSME was evaluated using simulated cross-sectional vascular RF data. The biomechanical design and the image-formation model used for this evaluation were described in Secs. II A and II C 3, respectively. The LSME elastograms were averaged over five independent realizations. Mean strain and shear values were averaged over selected ROIs in the elastograms to achieve quantitative comparisons between theoretical formulations and LSME results. Bias and relative error on the standard deviation (RESD) were computed for each component of the 2D-deformation matrix using the following equations:

$$\text{Bias} = \frac{\bar{\Delta}_{\text{LSME}} - \bar{\Delta}_{\text{Theory}}}{\bar{\Delta}_{\text{Theory}}} \times 100, \tag{13}$$

$$\text{RESD} = \frac{\sigma_{\text{LSME}} - \sigma_{\text{Theory}}}{\sigma_{\text{Theory}}} \times 100, \tag{14}$$

where $\bar{\Delta}_{\text{LSME}}$ and $\bar{\Delta}_{\text{Theory}}$ are the mean strain values estimated by the LSME and the theoretical solution within selected ROIs, respectively. Equivalently, σ_{LSME} and σ_{Theory} are the standard deviations respective to the LSME and the theory. It is worth mentioning that the standard deviation also includes *deformation decay*. (Deformation decay can be defined as a decreasing profile amplitude of Δ_{ij} from the inner to the outer vessel walls.) According to that, σ_{LSME} does not only reflect the accuracy of each implementation. Nevertheless, comparisons between methods are possible because the *deformation decay* is the same for all simulations. We decided not to remove the *deformation decay* because it is unknown for complex *in vitro* or *in vivo* vascular geometries.

III. RESULTS

III.A. Simulation data

Figure 3 presents the four Δ_{ij}-elastograms that were computed with the different implementations of the LSME, along with the theoretical elastograms. The colorbars express the strain and the shear in percent. Additional to *deformation decay*, mechanical artifacts[21] are also observed in these elastograms; that is because tissue motion occurs in the Lagrangian coordinate system, whereas the imaging system uses the Eulerian coordinate. In each case, comparisons with theory show qualitatively similar axial strain and shear distribution maps, whereas lateral deformation parameters remain questionable. Nevertheless, the ITER[c] implementation visually appears the best to map lateral elastograms. Due to the presence of strain and shear heterogeneities (decay and mechanical artifacts), quantitative comparisons were performed for specific ROIs, as identified by circles in the theoretical elastograms. Statistical comparisons were also performed, using one-way analysis of variance (ANOVA).

As a first quantitative comparison, Fig. 4 presents averages and standard deviations of each Δ_{ij} for the analytical and LSME elastograms with respect to ROIs identified in Fig. 3. Theory and LSME estimates show very good consistence for axial motion parameters, while LSME lateral motions presented larger biases and RESD. A more in-depth comparison is given in Table I, which exhibits the average, standard deviation, bias, and RESD of each Δ_{ij}. Regarding the axial deformation estimates, the bias was less than 33% in every case whereas it was less than 20% for the OF-based algorithm. For the axial strain parameter evaluated in the ROIs around 6 and 12 o'clock, the L&M method exhibited a minimum strain bias of -3% and was found to have statistically significant differences with any of the other three methods ($p < 0.001$). At the opposite, the L&M axial strain, which exhibited the worst bias around 3 and 9 o'clock at -32%, was also found statistically different from any of the other methods ($p < 0.001$). For the axial shear parameter, L&M and OF-based methods exhibited the smallest biases

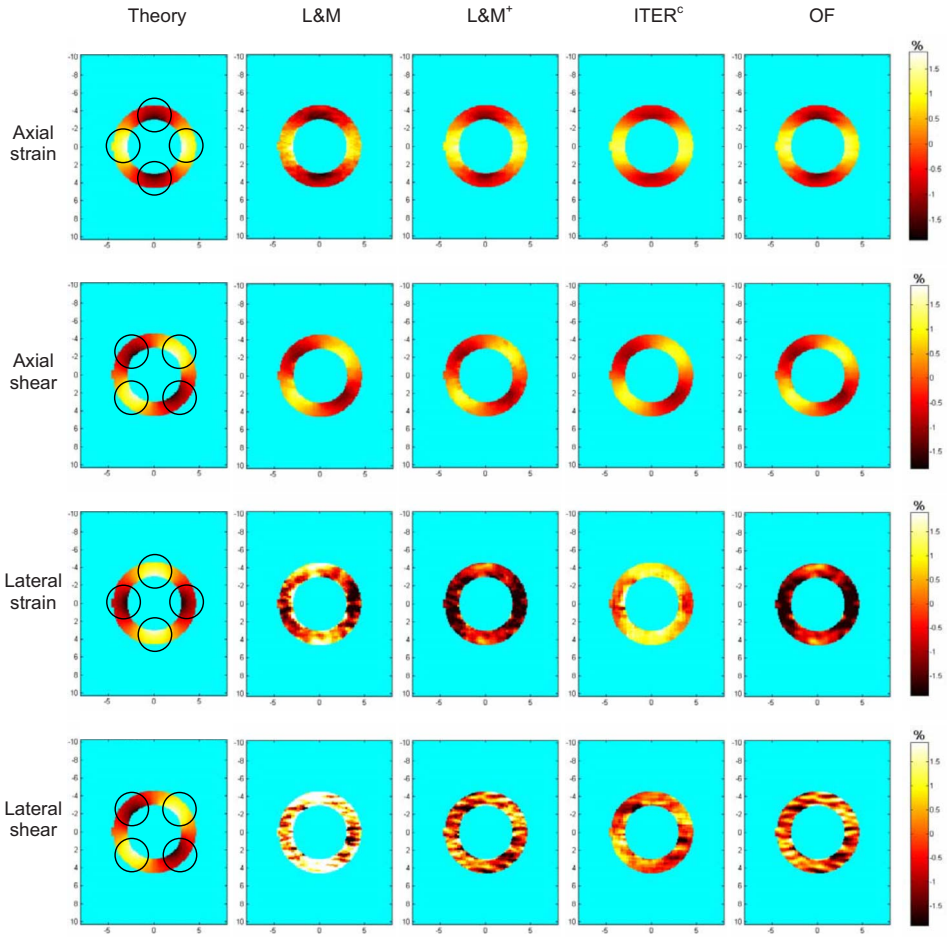

FIG. 3. Δ_{ij} elastograms computed with the analytical solution (left column) and with four implementations of the LSME for the simulation data. The colorbars express the strain and shear in percent. The circles in the left column identify the regions of interest where strains and shears were averaged.

(−17% and −19%, respectively) and were found to have statistically significant differences with L&M+ and ITERc ($p<0.001$). For the lateral strain around 6 and 12 o'clock, L&M and ITERc methods showed the lowest biases (15% and −8.5%, respectively) and were found statistically different from L&M+ and OF-based methods ($p<0.001$). For the lateral strain around 3 and 9 o'clock, the L&M, which exhibited the best bias (−20%) but the worst RESD, was found

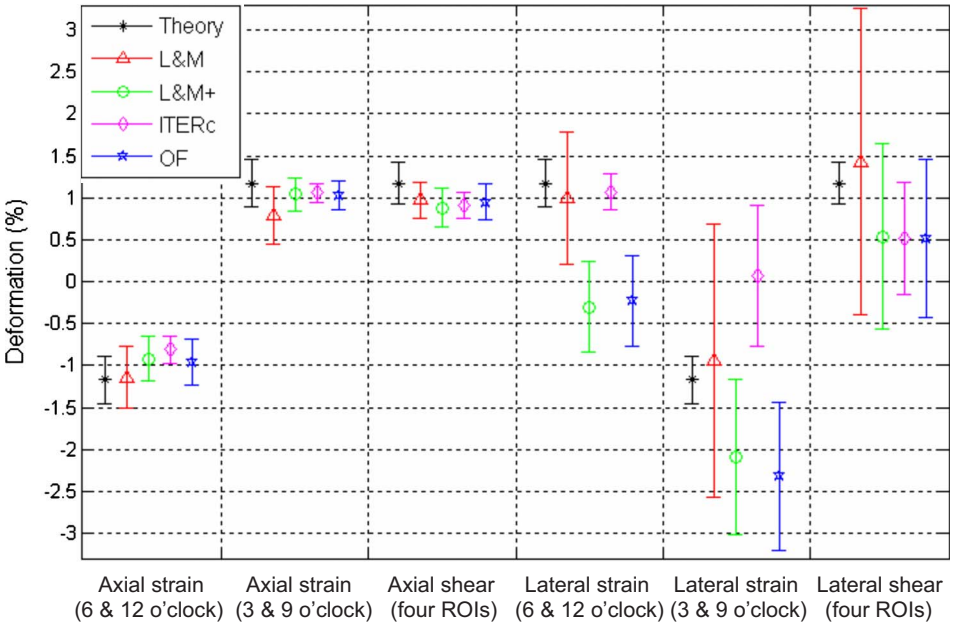

FIG. 4. Averages and standard deviations of each Δ_{ij} for the theoretical elastogram and LSME elastograms computed from simulated data.

TABLE I. Means, standard deviations (std), biases, and RESD on Δ_{ij} measured with the analytical solution and with the four implementations of the LSME for simulated data. The ROIs are given in Fig. 3.

			L&M		L&M$^+$		ITER^c		OF	
	Theory		Mean	std	Mean	std	Mean	std	Mean	std
	Mean	std	bias	RESD	bias	RESD	bias	RESD	bias	RESD
Motion parameters	%	%	%	%	%	%	%	%	%	%
Axial strain (6 and 12 o'clock)	−1.17	0.28	−1.14	0.37	−0.92	0.27	−0.81	0.16	−0.96	0.28
			−3	3×10^1	−21	−4	−31	−43	−18	0.0
Axial strain (3 and 9 o'clock)	1.17	0.28	0.79	0.35	1.04	0.20	1.06	0.11	1.03	0.17
			−32	3×10^1	−11	-3×10^1	−9.4	−61	−12	−39
Axial shear (four ROI)	1.17	0.25	0.97	0.22	0.88	0.23	0.91	0.15	0.95	0.21
			−17	-1×10^1	−25	−8	−22	−40	−19	-2×10^1
Lateral strain (6 and 12 o'clock)	1.17	0.28	0.99	0.79	−0.30	0.54	1.07	0.21	−0.23	0.54
			−15	1.8×10^2	-1.3×10^2	93	−8.5	-3×10^1	-1.2×10^2	93
Lateral strain (3 and 9 o'clock)	−1.17	0.28	−0.94	1.63	−2.09	0.92	0.07	0.84	−2.33	0.88
			−20	4.8×10^2	79	2.3×10^2	−106	2.0×10^2	99.1	2.1×10^2
Lateral shear (four ROI)	1.17	0.25	1.43	1.83	0.54	1.11	0.51	0.67	0.52	0.94
			22	6.3×10^2	−54	3.4×10^2	−56	1.7×10^2	−56	2.8×10^2

statistically different from any of the other methods ($p<0.01$). Similarly, for the lateral shear, the L&M exhibited the best bias (22%) but the worst RESD and was found statistically different from any of the other methods ($p\leq0.002$). The RESD values, which varied between −61% and 30% for the axial deformation estimates, were on average less than 40% for the OF-based algorithm with the axial strain RESD reaching 0% when the ultrasound beam runs in the same orientation as the tissue deformation. Except for the L&M, the RESD of the axial strain was worst around 3 and 9 o'clock where the ultrasound beam and the tissue motion were mostly orthogonally oriented. The RESD for lateral motion estimates was in most cases very high. This can mainly be explained by the baseband characteristics of the ultrasound system. With this regard, even though small biases could be measured, lateral motion estimates might not always be reliable in NIVE, when cross-sectional images are considered.

In summary, the L&M exhibited the lowest bias at −3% for axial strains around 6 and 12 o'clock, whereas OF-based method presented a 0% RESD. Around 3 and 9 o'clock, except for the L&M that exhibited the largest axial strain bias, the other three methods presented similar biases and RESD. Whereas the axial shear gave biases and RESD with similar ranges for most of the methods, L&M and OF-based methods were the best with less than 20% bias. Although ITER^c largely underestimated the RESD, presenting the worst scores for each axial motion parameter, it exhibited the most quantitatively reliable lateral strain estimates around 6 and 12 o'clock. For the 3 and 9 o'clock lateral strain and shear parameters, L&M presented the lowest biases but the highest RESD.

III.B. Phantom data

Figure 5 presents the four *in vitro* Δ_{ij}-elastograms that were computed, along with the theoretical elastograms for qualitative comparisons. The colorbars express the strain and the shear in percent. In most cases, the LSME produces axial strain and shear maps qualitatively similar to the theory. Additionally, the OF-based method generated smoother axial strain and shear elastograms than the other LSME methods. On the other hand, the lateral deformation components failed again in every LSME implementation.

IV. DISCUSSION

This paper reported a detailed review of the Lagrangian speckle model estimator (LSME) along with four different implementations, for applications in non-invasive vascular elastography (NIVE) of peripheral arteries. A homogeneous vessel wall, i.e., atherosclerotic-free, was investigated through numerical simulations and with a vessel-mimicking phantom.

IV.A. Simulation investigation

The image-formation model mimicked the Sonix RP scanner equipped with a 7 MHz linear array probe, whereas the physiological characteristics of an adult human subject were simulated. It was shown that every LSME underestimated the axial strain with a bias less than 33%. Many factors could contribute to such an underestimation, the first one being doubtless the measurement-window (MW). Indeed, because of the *deformation decay*, the maximum strain values take place at the inner wall. The MW then acts as a filter that cuts off such higher strain and shear values at the interface between the wall (site of correlated motion) and the lumen (site of highly uncorrelated motion). Additionally, motion estimate attenuation also originates from the image-formation model that uses a convolution operation and then smoothes the effective scatterers' movement. Finally, the point-spread function $[H(x,y)$ in Eq. (5)] includes a Gaussian term that may behave as an additional low-pass filter. Despite all those factors that contribute to decrease LSME motion estimates in comparison with theory, the LSME axial elastograms were

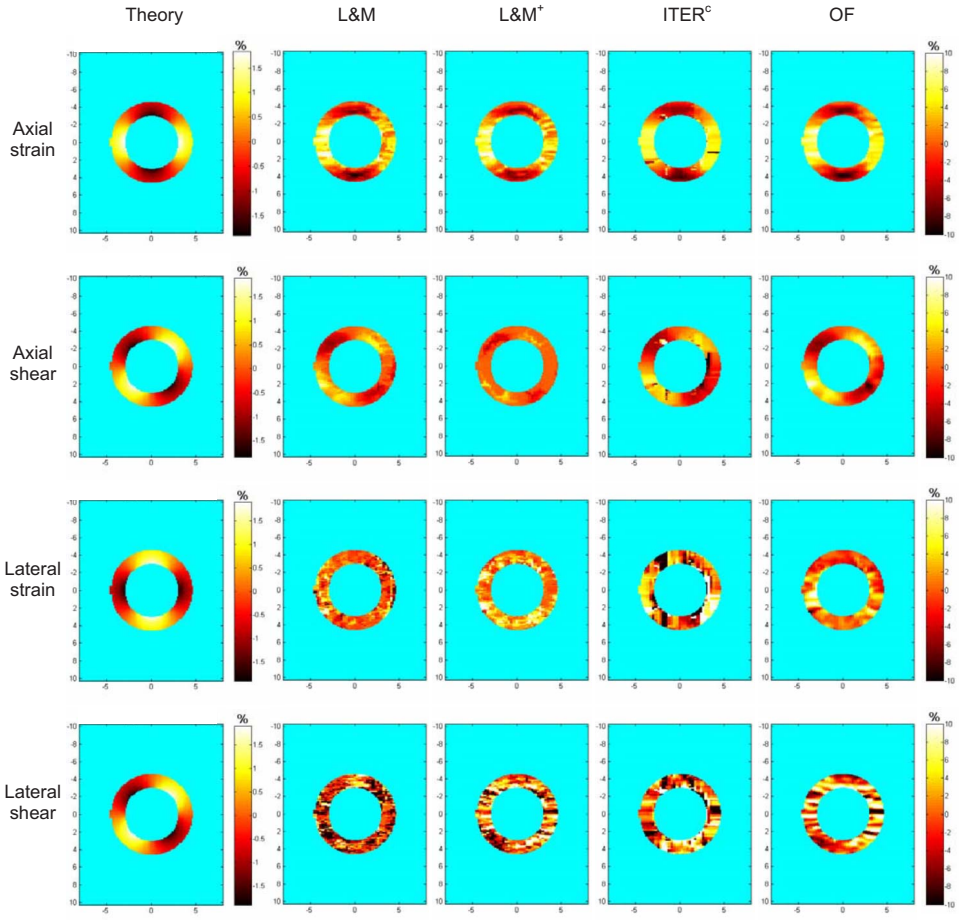

FIG. 5. Δ_{ij} elastograms computed with the analytical solution (left column) and with the four implementations of the LSME from the vessel-mimicking phantom data. The colorbars express the strain and shear in percent.

found qualitatively and quantitatively reliable. Whereas ITER^c was the implementation that exhibited the most reliable lateral strain estimates in cases where the ultrasound beam and the motion mostly run parallel, it exhibited the worst scores in terms of RESD [Eq. (14)] for each axial motion parameter. The fact that the standard deviation of ITER^c axial motion estimates is largely underestimated with respect to theory suggests that this method could be less sensitive to small changes in the strain pattern, thus reducing its ranges of strain and shear decays. A more in-depth comparison between the L&M and the L&M$^+$ shows that in general the better the bias for one, the worse the RESD. Additionally, it can be observed that L&M$^+$ and OF-based implementations provided very similar results. Indeed, except for the axial shear parameter, those methods showed good concordance ($p \geq 0.35$) as it could be expected. This is basically due to the fact that both algorithms use the OF equations to solve the minimization problem given in Eq. (8).

IV.B. Vessel-mimicking phantom investigation

Validation of NIVE was also performed with vessel-mimicking phantom experiments. Interestingly, it was shown that *in vitro* LSME axial strain and shear elastograms were also qualitatively similar to theory. Quantitatively speaking, the LSME axial deformation overestimated the theory, at least partially, due to the difficulty associated with having a perfect match between experimental and numerical conditions. Namely, it is very difficult to appropriately mimic precise geometries and mechanical properties with polyvinyl alcohol cryogel. On the other hand, as observed for the simulated data, lateral motion parameters remain questionable.

IV.C. Other considerations

Because of the limited lateral resolution of the acoustic aperture of most scanners, the lateral motion estimates were not reliable. Nevertheless, because biological soft tissues are assumed practically incompressible,[40] the lateral strain parameter could eventually be deduced from the axial one. In experimental situations (*in vitro* and *in vivo*), this was formulated as $\varepsilon_{xx} = -\varepsilon_{yy}/2$.[41] In such a case, only the lateral shear component would be of concern. Nevertheless, this can be seen as a coarse approximation of the lateral strain estimate with respect to the anisotropy of the vascular wall.

Whereas the four LSME implementations produced elastograms of about equivalent reliability, the OF-based algorithm remains an optimal choice since it improves the elastograms' computation time relative to the original L&M by a factor of roughly 150 while an improvement factor of approximately 33 was noted with respect to the L&M$^+$ and ITER^c.

On the other hand, other groups reported the Cramer-Rao lower bound (CRLB)[42] and the strain filter[43,44] to quantify the reliability of motion estimates. Nevertheless, such theoretical frameworks were developed around correlation-based motion estimators instead of minimization-based methods, as it is the case for the LSME, and would not have been appropriate in the context of this study.

IV.D. NIVE clinical applications

Whereas NIVE was found reliable with regards to the assessment of axial motion parameters, many other factors could impair such a reliability in clinical applications. Namely, motion estimates can be subjected to geometrical biases that tend to decrease strain estimates. Indeed, this can be seen as similar, by analogy, to angle-dependent Doppler velocity measurements. It is worth noting that geometric biases stem from divergences between tissue motion and ultrasound beam propagation orientations. In such a case, strategies for angle-dependent strain correction could be required. NIVE reliability can also be impaired by motion artifacts originating from patient breathing or swallowing. Finally, the external stress applied by the radiologist with the probe could act as a preload on the vessel wall that modulates strain estimates.[20]

V. CONCLUSIONS

Whereas NIVE has yet been shown to be a promising method to characterize peripheral arteries,[21,23,41] this paper overviews four different implementations of the Lagrangian speckle model estimator (LSME) for such an application. For each algorithm, simulated and vessel-mimicking phantom data provided axial strain and shear elastograms that were qualitatively similar to theory and quantitatively reliable. Because the optical flow-based LSME outperforms the other implementations by a factor higher than 30 in terms of processing time, and because of its reliability to compute both axial strain and shear motion parameters, it can be promoted as an optimal choice for further applications in non-invasive vascular elastography. To conclude, it is worth remembering that whereas axial strain elastograms might help identifying plaque components, axial shears might give insights about plaque vulnerability. This could be of clinical significance in the cardiovascular field, thanks to the LSME.

ACKNOWLEDGMENTS

The financial support for this research was provided by the Natural Sciences and Engineering Research Council of Canada (NSERC Grant No. 312136-06) and by the Collaborative Health Research Program of NSERC and the Canadian Institutes of Health Research (NSERC Grant No. 323405-06 and CIHR Grant No. CPG-80085). G.C. is a recipient of the National Scientist award of the Fonds de la Recherche en Santé du Québec (FRSQ, 2004–2009). The salary of R.L.M. is partially supported by a research scholarship from FRSQ.

[a]Author to whom correspondence should be addressed. Electronic mail: maurice.roch.chum@ssss.gouv.qc.ca

[1]R. Stocker and J. F. Keaney, Jr., "Role of oxidative modifications in atherosclerosis," Physiol. Rev. **84**, 1381–1478 (2004).
[2]V. Fuster, P. R. Moreno, Z. A. Fayad, R. Corti, and J. J. Badimon, "Atherothrombosis and high-risk plaque: part I: evolving concepts," J. Am. Coll. Cardiol. **46**, 937–954 (2005).
[3]A. W. Clowes and S. A. Berceli, "Mechanisms of vascular atrophy and fibrous cap disruption," Ann. N. Y. Acad. Sci. **902**, 153–162 (2000).
[4]C. J. Slager, J. J. Wentzel, F. J. Gijsen, J. C. Schuurbiers, A. C. van der Wal, A. F. van der Steen, and P. W. Serruys, "The role of shear stress in the generation of rupture-prone vulnerable plaques," Nat. Clin. Pract. Cardiovasc. Med. **2**, 401–407 (2005).
[5]C. J. Slager, J. J. Wentzel, F. J. Gijsen, A. Thury, A. C. van der Wal, J. A. Schaar, and P. W. Serruys, "The role of shear stress in the destabilization of vulnerable plaques and related therapeutic implications," Nat. Clin. Pract. Cardiovasc. Med. **2**, 456–464 (2005).
[6]J. M. U-King-Im, Z. Y. Li, R. A. Trivedi, S. Howarth, M. J. Graves, P. J. Kirkpatrick, and J. H. Gillard, "Correlation of shear stress with carotid plaque rupture using MRI and finite element analysis," J. Neurol. **253**, 379–381 (2006).
[7]M. Cinthio, A. R. Ahlgren, J. Bergkvist, T. Jansson, H. W. Persson, and K. Lindstrom, "Longitudinal movements and resulting shear strain of the arterial wall," Am. J. Physiol. Heart Circ. Physiol. **291**, H394–H402 (2006).
[8]H. E. Talhami, L. S. Wilson, and M. L. Neale, "Spectral tissue strain: a new technique for imaging tissue strain using intravascular ultrasound," Ultrasound Med. Biol. **20**, 759–772 (1994).
[9]B. M. Shapo, J. R. Crowe, A. R. Skovoroda, M. J. Eberle, N. A. Cohn, and M. O'Donnell, "Displacement and strain imaging of coronary arteries with intraluminal ultrasound," IEEE Trans. Ultrason. Ferroelectr. Freq. Control **43**, 234–246 (1996).
[10]L. K. Ryan and F. S. Foster, "Ultrasonic measurement of differential displacement and strain in a vascular model," Ultrason. Imaging **19**, 19–38 (1997).
[11]É. Brusseau, J. Fromageau, G. Finet, P. Delachartre, and D. Vray, "Axial strain imaging of intravascular data: results on polyvinyl alcohol cryogel phantoms and carotid artery," Ultrasound Med. Biol. **27**, 1631–1642 (2001).
[12]C. L. de Korte, M. J. Sierevogel, F. Mastik, C. Strijder, J. A. Schaar, E. Velema, G. Pasterkamp, P. W. Serruys, and A. F. van der Steen, "Identification of atherosclerotic plaque components with intravascular ultrasound elastography *in vivo*: a Yucatan pig study," Circulation **105**, 1627–1630 (2002).
[13]R. L. Maurice, É. Brusseau, G. Finet, and G. Cloutier, "On the potential of the Lagrangian speckle model estimator to characterize atherosclerotic plaques in endovascular elastography: *in vitro* experiments using an excised human carotid artery," Ultrasound Med. Biol. **31**, 85–91 (2005).
[14]R. L. Maurice, J. Fromageau, É. Brusseau, G. Finet, G. Rioufol, and G. Cloutier, "On the Potential of the Lagrangian Speckle Model Estimator for Endovascular Ultrasound Elastography: In vivo Human Coronary Study," Ultrasound Med. Biol. **33**, 1199–1205 (2007).
[15]J. A. Schaar, C. L. de Korte, F. Mastik, L. C. van Damme, R. Krams, P. W. Serruys, and A. F. van der Steen, "Three-dimensional palpography of human coronary arteries. Ex vivo validation and in-patient evaluation," Herz **30**, 125–133 (2005).
[16]R. L. Maurice, J. Fromageau, M. Doyley, E. Demuinck, J. Robb, and G. Cloutier, "Characterization of atherosclerotic plaques with intravascular ultrasound elastography: a rabbit model study," Medical Image Computing and Computer-Assisted Intervention (MICCAI), Workshop on Computer Vision for Intravascular and Intracardiac Imaging (CVII) (2006), pp. 6–13.
[17]J. J. Mai and M. F. Insana, "Strain imaging of internal deformation," Ultrasound Med. Biol. **28**, 1475–1484 (2002).
[18]J. Bang, T. Dahl, A. Bruinsma, J. H. Kaspersen, T. A. Hernes, and H. O. Myhre, "A new method for analysis of motion of carotid plaques from RF ultrasound images," Ultrasound Med. Biol. **29**, 967–976 (2003).
[19]H. Kanai, H. Hasegawa, M. Ichiki, F. Tezuka, and Y. Koiwa, "Elasticity imaging of atheroma with transcutaneous ultrasound: preliminary study," Circulation **107**, 3018–3021 (2003).
[20]K. Kim, W. F. Weitzel, J. M. Rubin, H. Xie, X. Chen, and M. O'Donnell, "Vascular intramural strain imaging using arterial pressure equalization," Ultrasound Med. Biol. **30**, 761–771 (2004).

[21]R. L. Maurice, J. Ohayon, Y. Frétigny, M. Bertrand, G. Soulez, and G. Cloutier, "Non-invasive vascular elastography: theoretical framework," IEEE Trans. Med. Imaging **23**, 164–180 (2004).
[22]H. Ribbers, R. G. Lopata, S. Holewijn, G. Pasterkamp, J. D. Blankensteijn, and C. L. de Korte, "Noninvasive two-dimensional strain imaging of arteries: validation in phantoms and preliminary experience in carotid arteries in vivo," Ultrasound Med. Biol. **33**, 530–540 (2007).
[23]C. Schmitt, G. Soulez, R. L. Maurice, M. F. Giroux, and G. Cloutier, "Non-invasive vascular elastography: toward a complementary characterization tool of atherosclerosis in carotid arteries," Ultrasound Med. Biol. **33**, 1841–1858 (2007).
[24]G. E. Trahey, M. L. Palmeri, R. C. Bentley, and K. R. Nightingale, "Acoustic radiation force impulse imaging of the mechanical properties of arteries: in vivo and ex vivo results," Ultrasound Med. Biol. **30**, 1163–1171 (2004).
[25]D. Dumont, R. H. Behler, T. C. Nichols, E. P. Merricks, and C. M. Gallippi, "ARFI imaging for noninvasive material characterization of atherosclerosis," Ultrasound Med. Biol. **32**, 1703–1711 (2006).
[26]J. Krejza, M. Arkuszewski, S. E. Kasner, J. Weigele, A. Ustymowicz, R. W. Hurst, B. L. Cucchiara, and S. R. Messe, "Carotid artery diameter in men and women and the relation to body and neck size," Stroke **37**, 1103–1105 (2006).
[27]R. Kazmierski, C. Watala, M. Lukasik, and W. Kozubski, "Common carotid artery remodeling studied by sonomorphological criteria," J. Neuroimaging **14**, 258–264 (2004).
[28]J. Fromageau, J. L. Gennisson, C. Schmitt, R. L. Maurice, R. Mongrain, and G. Cloutier, "Estimation of polyvinyl alcohol cryogel mechanical properties with four ultrasound elastography methods and comparison with gold standard testings," IEEE Trans. Ultrason. Ferroelectr. Freq. Control **54**, 498–509 (2007).
[29]R. L. Maurice and M. Bertrand, "Lagrangian speckle model and tissue-motion estimation- theory," IEEE Trans. Med. Imaging **18**, 593–603 (1999).
[30]B. K. P. Horn, *Robot Vision* (McGraw-Hill, New York, 1986), pp. 278–298.
[31]F. Kallel, M. Bertrand, and J. Meunier, "Speckle motion artifact under tissue rotation," IEEE Trans. Ultrason. Ferroelectr. Freq. Control **41**, 105–122 (1994).
[32]R. L. Maurice and M. Bertrand, "Speckle motion artifact under tissue shearing," IEEE Trans. Ultrason. Ferroelectr. Freq. Control **46**, 584–594 (1999).
[33]J. Meunier and M. Bertrand, "Ultrasonic texture motion analysis: theory and simulation," IEEE Trans. Med. Imaging **14**, 293–300 (1995).
[34]J. Ophir, S. K. Alam, B. Garra, F. Kallel, E. Konofagou, T. Krouskop, and T. Varghese, "Elastography: ultrasonic estimation and imaging of the elastic properties of tissues," Proc. Inst. Mech. Eng., Part H: J. Eng. Med. **213**(3), 203–233 (1999).
[35]P. Chaturvedi, M. F. Insana, and T. J. Hall, "2-D companding for noise reduction in strain imaging," IEEE Trans. Ultrason. Ferroelectr. Freq. Control **45**, 179–191 (1998).
[36]P. Chaturvedi, M. F. Insana, and T. J. Hall, "Testing the limitations of 2-D companding for strain imaging using phantoms," IEEE Trans. Ultrason. Ferroelectr. Freq. Control **45**, 1022–1031 (1998).
[37]R. L. Maurice, J. Ohayon, G. Finet, and G. Cloutier, "Adapting the Lagrangian speckle model estimator for endovascular elastography: theory and validation with simulated radio-frequency data," J. Acoust. Soc. Am. **116**, 1276–1286 (2004).
[38]K. Levenberg, "A method for the solution of certain nonlinear problems in least-squares," Q. J. Appl. Math. **2**(2), 164–168 (1944).
[39]D. W. Marquardt, "An algorithm for least-squares estimation of nonlinear parameters," J. Soc. Ind. Appl. Math. **11**, 431–441 (1963).
[40]T. A. Krouskop, D. R. Dougherty, and F. S. Vinson, "A pulsed Doppler ultrasonic system for making noninvasive measurements of the mechanical properties of soft tissue," J. Rehabil. Res. Dev. **24**, 1–8 (1987).
[41]R. L. Maurice, M. Daronat, J. Ohayon, E. Stoyanova, S. Foster, and G. Cloutier, "Non-invasive high-frequency vascular ultrasound elastography," Phys. Med. Biol. **50**, 1611–1628 (2005).
[42]E. E. Konofagou, T. Varghese, and J. Ophir, "Theoretical bounds on the estimation of transverse displacement, transverse strain and Poisson's ratio in elastography," Ultrason. Imaging **22**, 153–177 (2000).
[43]T. Varghese and J. Ophir, "The nonstationary strain filter in elastography: Part I. Frequency dependent attenuation," Ultrasound Med. Biol. **23**, 1343–1356 (1997).
[44]F. Kallel, T. Varghese, J. Ophir, and M. Bilgen, "The nonstationary strain filter in elastography: Part II. Lateral and elevational decorrelation," Ultrasound Med. Biol. **23**, 1357–1369 (1997).